A shape optimization procedure for cylinders aeolian tone

Wagner J. G. S. Pinto, Florent Margnat

To cite this version:

Wagner J. G. S. Pinto, Florent Margnat. A shape optimization procedure for cylinders aeolian tone. 2018. hal-01844771

HAL Id: hal-01844771
https://hal.science/hal-01844771

Preprint submitted on 19 Jul 2018

A shape optimization procedure for cylinders aeolian tone

Wagner José Gonçalves da Silva Pinto, Florent Margnat[1]

Intitute PPRIME, Department of Fluid Flow, Heat Transfer and Combustion, Université de Poitiers - ENSMA - CNRS,
Building B17 - 6 rue Marcel Doré - TSA 41105 86073, POITIERS CEDEX 9, France

---

Abstract

A shape optimization procedure is presented. It is dedicated to the noise generated by obstacle flows. The cost function is the acoustic power efficiency, which is derived directly from the fluctuations of the aerodynamic force through for a single formula from the hypothesis of tonal noise. The force is estimated from the direct solution of the 2D incompressible, unsteady flow in laminar regime over a convex symmetrical obstacle without incidence. The no-slip condition at the boundary is assured by an Immersed Boundary Method, that allows the use of the same mesh for all the geometries. The shape of the obstacle is defined by 4 Bézier curves, constrained by second-order continuity leading to 4 degrees of freedom: the aspect ratio, the position of the maximum cross section and two curvature parameters (up and downstream). The optimization is performed via a Particle Swarm Optimization (PSO) routine. Several tests are performed increasing complexity so that coefficients of the PSO be adjusted to the present response surface. There is up to 16 dB of difference between the power efficiency of the extrema configurations for a fixed aspect ratio (AR) and 8 dB for constrained surface or perimeter. For an AR of 1.5, the optimal shape leads to 3dB less acoustic power than the ellipse of same AR. The shapes that minimize acoustic power are relatively different from those that minimize the mean drag.

Keywords: aeroacoustics, airframe noise, shape optimization, Particle Swarm Optimization, Immersed Boundary Method

---

1. Introduction

The use of optimization for aerodynamic design is reported many times in the literature. When the physics of the problem is not well defined or too complex to be fully predicted, such as in most fluid mechanics applications, it is clear that optimization is the most direct way to define the best parameters under a set of criteria and weighted objectives. Although being fairly represented with different test cases and conditions, the reported results are restricted to the use of physical models under severe restrictions (turbulence models, steady flow) and approximations for the response surfaces. Additionally, there is not much accounting for the aeroacoustics behavior of the flow.

In that sense, we may highlight two aspects associated with the interaction with a body with a flow: noise and vibration. Those two major issues in modern engineering have a tremendous effects in health and the occupation of the urban space. In this context, the comprehension and discussion of adapted optimization techniques for aerodynamics and aeroacoustics fulfills industrial and environmental demands, specially on the transports field.

Apart of classical derivative based optimizers, meta-heuristic techniques work with the objective function being a black box. No previous knowledge of the behavior of the function or the response surface must exist in order to achieve a converging point, only the evaluation of point-wise calculations. Most interesting aspect of this kind of optimizer is the capability to be set to find global extrema and in general, easy implementation and parallel evaluation.

Most of those optimizers are a reproduction of a natural phenomenon, such as the Darwin's theory of biological evolution (Genetic Algorithms [1] - GA, Differential Evolution [2] - DE) and the social behavior of animals (Ant Colony Optimization

---

[1] Corresponding author: florent.margnat@univ-poitiers.fr

[3] - ACO, Particle Swarm Optimization [4] - PSO). Many previous uses of this family of optimizers in the field of aerodynamics is found on the literature, we highlight some recent articles: the shape optimization of high-speed trains of Krajnovic [5]; the optimization of wings of Praveen and Duvigneau [6], the aerodynamic and aeroacoustic optimization of an extended Ahmed body of Beigmoradi et al. [7]; and the high speed train nose optimization of Yao and al. [8].

Study object of this paper are bluff bodies, a category of geometries common in many applications and of great interest in academic context once they can be a test case for turbulence, aeroacoustics and instability analysis. A geometry can be considered optimal for presenting either the minimum (reduced noise and fatigue) or the maximum (for energy harvesting) force oscillations. From the authors' knowledge, the full description of a bluff body wake at low Reynolds remains unclosed despite the effort of many authors along the history [9, 10].

As far as aeroacoustics or vibration are targeted, the description of the unsteady phenomena within the flow is requested. However, such description at the regimes of most of the engineering applications needs too much computational effort, which prevents hundreds simulations, necessary for the optimization process, to be conducted without any modeling strategy. In the present approach, the numerical estimation of the objective function relies on unsteady simulations of bluff body flows in the 2D, laminar regime. Indeed, even at high Reynolds numbers (excepted around the drag crisis) the vortex shedding is the highly emerging element in the acoustic spectrum ([11, 12], see also [13]). Therefore, the laminar flow is considered as a good representation of the global mode of the wake which is relevant regarding acoustics and which will persist at higher Reynolds number. However, broadband components, as well as its relative level with respect to the tonal components, cannot be included in the present approach.

The direct numerical solution of the incompressible Navier-Stokes equations uses the Immersed Boundary Method (IBM), modeling the no-slip condition with an external force field [14]. Due to its flexibility, it's mostly used for simulations of complex geometries and of fluid-structure interaction [15]. An application of IBM in an aeroacoustic context was conducted in [16]. The interest of applying it for the optimization of static and relatively simple shapes remains in the fact that modifying the geometry is a simple task and re-meshing or mesh deformation steps, such as the spring analogy method [17] or radial functions interpolation [18], are not necessary. The acoustic calculations are based on an hybrid method: the aerodynamic solution is used as an input for a model based on Curle's development [19] of Lighthill's acoustical analogy [20]. As only an explicit scalar formula is used to estimate the acoustic power of each geometry, the aerodynamic solution is the most expensive element of the optimization framework, which is based on a PSO routine.

The paper is organized as follows. Section 2 is dedicated to describing the methodology of the numerical solver for the aerodynamic and acoustic fields, the optimization technique and a study of its settings and the test case geometry. Section 3 contains the results of the application of the proposed framework. Final remarks and perspectives conclude the document.

2. Methodology

2.1. Acoustic model

As the criterion for optimizing the total, tonal noise emission by the flow over a body, the acoustic power W is selected.

From Curle integral solution [19] in the frequency domain, assuming a compact source, considering only the first non-vanishing modes of the Fourier transform of the acoustic intensity and neglecting the influence of the motion in the observer domain, an analytical expression was derived by [21] as:

$$W = \frac{\pi}{16}\rho_0 U_\infty^3 d \mathrm{St}\mathrm{M}^2 (2{C'_D}^2 + {C'_L}^2) \qquad (2.1)$$

where W is the acoustic power (integral of the acoustic intensity over an observer circle of arbitrary radius in the far field), ρ_0 is the density in the propagation medium, U_∞ is the upstream velocity, d its the main cross section. The Strouhal number St is based on U_∞, d, and the main frequency of lift fluctuations. Noting c_0 the sound velocity, $\mathrm{M} = U_\infty/c_0$ is the Mach number. C'_D and C'_L are the period's root mean square (RMS) of the fluctuations of the drag and lift coefficients (per unit length):

$$C_D = \frac{F_1}{\frac{1}{2}\rho_0 U_\infty^2 d} \qquad C_L = \frac{F_2}{\frac{1}{2}\rho_0 U_\infty^2 d} \qquad (2.2)$$

where F_1 and F_2 are the components of the aerodynamic effort on the directions y_1 and y_2, respectively, as displayed on Figure 1.

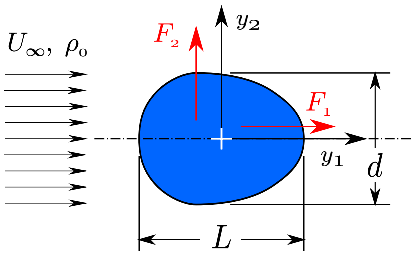

Figure 1: Problem definition.

Since $\rho_0 U_\infty^3 d$ represents the reference power (by unit length) supplied by the incoming flow, all results presented on this article are for the non-dimensional acoustical power W_a, quantifying an acoustic efficiency:

$$W_a = W/\rho_0 U_\infty^3 d \tag{2.3}$$

Once all the simulations are incompressible, the Mach number is chosen arbitrarily. The value M = 0.1 is set, consistently with the assumptions of the model. This quantity is the only acoustical evaluation performed for every geometry. It's interesting to analyze the obstacle in terms of acoustic emission as this combines the influence of both the Strouhal and the fluctuations of the aerodynamic efforts.

2.2. Aerodynamic solver

The flow is numerically predicted by solution of the incompressible Navier-Stokes equation in 2D. The numerical code uses a 6^{th}-order, compact centered finite difference scheme for the evaluation of space derivatives, and a 3^{rd}-order Runge–Kutta time-marching scheme. That solver is described in details in [22].

Solid domain is modeled by the IBM method where a forcing term $\mathbf{f}$ is added to the momentum equation [14, 23]:

$$\begin{gathered}\frac{\partial \mathbf{u}}{\partial t} + \mathbf{u}_j \frac{\partial \mathbf{u}_i}{\partial y_j} = -\frac{\partial}{\partial y_j}[p\delta_{ij} - \tau_{ij}] + \mathbf{f} \\ \mathbf{f}(\mathbf{y}, t) = -\epsilon(\mathbf{y}) \left[\omega_n^2 \int \mathbf{u}(\mathbf{y}, t) dt + 2\zeta\omega_n \mathbf{u}(\mathbf{y}, t)\right]\end{gathered} \tag{2.4}$$

where, ω_n is the natural frequency and ζ is the damping coefficient of the second order controller that forces a null velocity everywhere ϵ is non zero. On this work, the IBM coefficients are $\omega_n = 50$ and $\zeta = 1$, based on [23].

Selection of the solid and fluid domains is based on the position of each node: $\epsilon = 1$ (forced grid points) if the node is inside the analytical contour and $\epsilon = 0$ elsewhere, as illustrated by the circles and triangles in the Figure 2 a). In the current work, there is no interpolation of the forcing term for refining the boundaries.

Although the easy utilization, it imposes a limitation in the geometrical precision of the curves as big as the cells size as can be seen on Figure 2. For the chosen refinement, more details on Appendix A.2, there are 26 cells in a distance of length $1d$.

In the present context, the IBM also yields a simple way to estimate the aerodynamic effort, through volume integral of the source term $\mathbf{f}$ over the solid domain, as derived in [21].

The Cartesian grid is uniform streamwise, while, in the transverse direction, it is stretched from the body center, the later being taken as the origin of the reference frame. Free-slip conditions are set at the lateral boundaries of the computational domain, while a convection condition is set outflow.

Once all the simulations are done in 2D, it is possible that the flow for some specific geometries is already tridimensional. These effects are not taken in account in the simulation. The presented values are for simulations with Reynolds number $Re = U_\infty d/\nu$ of 150, being the obstacle's total height d the characteristic length and ν the kinematic viscosity. That regime ensures unsteadiness for all the bodies with length smaller than $3d$. Moreover, it is a standard value from literature, with, for instance, direct noise computation for circular [24] and rectangular [25] cylinders.

Regarding the grid, a careful convergence study has been conducted for generic shapes, in order to obtain a fruitful trade-off between low estimation time of the unsteady flow statistics and errors. Indeed, the objective here is to correctly describe the influence of the body shape, whose variety causes a large range of reported aerodynamic coefficients. Thus, based on the tests reported in Appendix A.2, the domain is set $25d$ long streamwise and $20d$ in spanwise direction, and discretized in 649 × 257 nodes. The center of the geometry is at $11d$ from the inflow boundary, at the middle in the transverse direction.

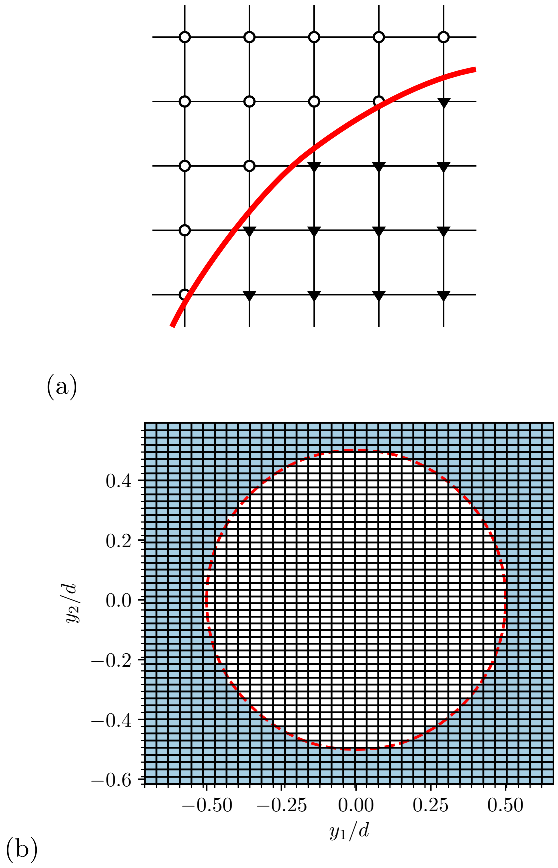

Figure 2: (a) Definition of fluid and solid domains based on nodes position, represented by the circles and triangles, respectively; the thick line is the analytical contour of the modeled shape; (b) Fluid (filled) and solid domains for the circular cylinder of radius d/2, analytical geometry is represented by the dashed line, for better visualization, the cells are centered on the nodes on this representation.

The initial condition is $(u_1, u_2) = (U_\infty, 0)$ everywhere. After the transient during which the velocity goes to zero in the solid domain and the wake is established, the periodic flow is obtained. The optimization process requires that the simulation for a given geometry stops after convergence without human intervention. The definition of a criterion based on the aerodynamic coefficients convergence (for instance, less than 1% variation between two subsequent periods) was hardly found as universal for all the geometries. A constant, large enough number of iterations was preferable, thus, for every simulation, the physical time is about $360d/U_\infty$, corresponding to 50,000 timesteps $\Delta t = 0.0072d/U_\infty$, and about 50 lift periods.

With such settings, a single simulation of one body shape is completed within two hours, enabling about thirty runs to be conducted successively within three days. This is the starting point when an optimization procedure is planed, requesting several objective function estimations.

2.3. Parametrized geometry

Now that the objective function computation has been described for a given geometry, the next step in the design of the optimization process is the space of parameters describing how the geometry can vary. In order to be consistent from the aerodynamic point of view, the blocking height, d, of the body is kept constant and is the reference length of the problem. Also, except at the boundaries of the parameter space, second-order continuity is desired so that acceleration of fluid particles be finite. Moreover, focusing on the influence of shape on the acoustic efficiency, only symmetric bodies without incidence are considered, avoiding consideration about mean lift, which is null by construction. Finally, although some interesting solutions could be got by concave shapes, these would form cavities, thus greatly complicating the aeroacoustic problem through possible acoustic feedbacks and whistling, in particular as the Reynolds number is increased. That is why the present study is restricted to convex shapes.

A first parameter strongly influencing both the mean and unsteady flow is the aspect-ratio L/d. Once it is fixed, this form a rectangle that circumscribes the body. Within this, the next relevant parameter is the position of the maximum cross section. Here, this is controlled by k, such that the maximum cross section is at kL. Finally, one may want to adjust the curvature of the front part and the back part separately. For that purpose, two parameters are introduced: j_F and j_B, allowing to change continuously from a lozenge ($j_B = j_F = 0$) to a rectangle ($j_B = j_F = 1.0$).

Accounting for all of these aerodynamic and geometrical constraints, the generic shape used in this optimization study is built from 4 Bézier curves in each hemisphere, two quadratic at the leading and trailing end, and two cubic connected at the main cross section. The full description of the geometry is at the Appendix B.1. Figure 3 illustrates some of the geometries that can be obtained varying k, j_B and j_F. For the sake of completeness, note that half an ellipse is drawn when j_B or j_F equals $\sqrt{2} - 1$.

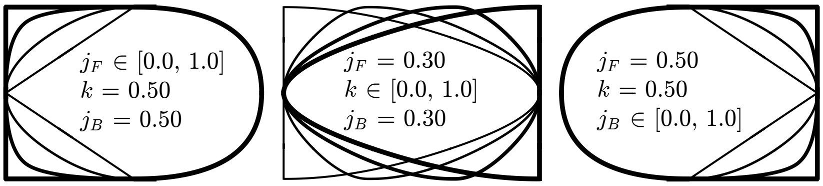

Figure 3: Possible shapes for fixed aspect ratio ($L/d = 1.5$) and varying j_F (left), k (center) and j_B (right) between 0 and 1 (thickest curve is for the maximum value of the varying parameter).

With the use of IBM, there is no need to re-mesh after every parameters modification. The mesh is a Cartesian grid that is unchanged and independent of the geometry and, for every evaluation, only the array $\epsilon(\mathbf{y})$ in Equation 2.4 is updated.

2.4. Optimization method

Optimization is performed using the Particle Swarm Optimization. Introduced by Kennedy and Eberhart [4], it mimics the social behavior of a flock of animals (originally birds) when they look for a common objective, such as food.

Consider a swarm composed by n agents (also called particles), placed arbitrarily on a design space of dimension D. A random initial velocity is defined for every agent and the objective function is calculated for all of them. The coordinates of best result for the group of agents in the first iteration is defined as g_i, for $i = 1, ..., D$. The position at the following iteration ($T + 1$) is a function of the distance of each particle from its own best ($p_i - x_{i,T}$), the distance from the swarm's best (g_i $- x_{i,T}$), and its current velocity ($v_{i,T}$):

$$\begin{cases} v_{i,T+1} = c_w v_{i,T} + c_1 r_1 (p_i - x_{i,T}) + c_2 r_2 (g_i - x_{i,T}) \\ x_{i,T+1} = x_{i,T} + v_{i,T+1} \end{cases} \tag{2.5}$$

where c_w is the inertial factor (later introduced by Shi and Eberhart [26]), that regulates the influence of previous velocity on the particle movement, c_1 and c_2 are the cognitive and social factor, respectively, that represents the influence of the distance to the personal and the swarm's best fitness location, r_1 and r_2 are normally distributed random number between 0 and 1. The function evaluation is performed and the position of personal and swarm bests are updated. Those steps are repeated iteratively until the stopping criteria is reached (maximum number of iterations or value of error, for example).

In the present application, when the particles reach outside of the design space, they are simply repositioned to the limits without any modification on the velocity. More elaborated strategies are reported on the literature.

The *gbest* topology (communication structure) is used here, meaning all particles are aware of the personal best of every member of the swarm. The convergence is faster but the design space is not explored as much as for other topologies where information is restricted to subgroups of particles.

The version of PSO used on this work is very close to the canonical due to its simplicity and robustness. Many improvements have been made to the technique and the reader is invited to look at [27] for an extensive description. A description of the used environment is on the following section.

2.4.1. Optimization framework

The optimization is implemented in Python, while the aerodynamic solver is based on Fortran. As the objective function requires the resolution of the unsteady Navier Stokes equations, the considered result is derived from the statistics of the last complete flow cycle that was simulated, based on the two final peaks on the lift signal (for this regime, the aerodynamic efforts are clean sinusoidal signals).

Each simulation is single cored, and for every iteration, the n agents are evaluated simultaneously in a cluster. As illustrated on Figure 4, the parallelism is done using the MPI standard with the package mpi4py [28]. For 36 particles (that means 36 simultaneous simulations) the calculation time for each geometry increases from 2 hours to about 3 hours on the regional high-performance computing facility. This imperfect speed-up may be due to memory access issues.

Convergence of the swarm could be accelerated using information acquired by other particles in the

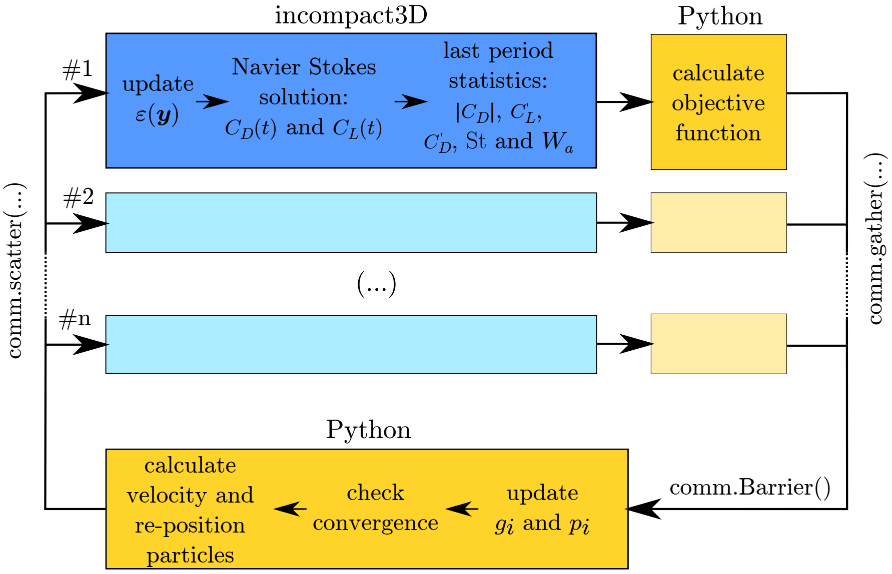

Figure 4: Optimization framework. For a given iteration, the geometrical parameters of the particles are scattered into n MPI process using mpi4py method scatter, where comm is the main communicator. After the simulations are completed, data is sent to the main process using the method gather, the best local and global position are updated and the particles are moved if there isn't swarm convergence or the maximum number of iterations is not reached.

current iteration [29]. However, this can not be implemented here because of the parallel implementation. Which leads the best swarm's position and each particle status (personal best, velocity and position) to be updated only after a complete iteration.

As the geometry is discretized to a number of rectangular elements based on their coordinates in a Cartesian mesh, small variations on the geometrical parameters do not affect the simulated geometry. For the size element used in this work (see Appendix A.2), the minimum sensibility is of 0.001 for any parameter. Therefore, all the inputs are rounded when calling the Navier Stokes solver (the value is unchanged in the optimization routine). In order to avoid unnecessary calls, if the same set of parameters has been used before in the optimization, the previously calculated value is considered and the simulation is not performed. At the final iterations, as the swarm converges, the number of actual function evaluations per iteration is highly reduced, specially for a 2D search space.

As discussed by many authors, choosing the optimization parameters is the main difficult for the use of a meta-heuristic optimizer such as PSO [29, 27, 30]. Even though convergence can be achieved based on values in the literature, they are mostly adapted for solving hard problems [31]. In order to find parameters adapted to the present context (the ones that result in a small number of objective function evaluations/iterations), empirical tests are prepared regarding response surfaces and performances.

2.4.2. Test Response Surfaces

Once the general shape of the objective functions is known, the optimizer's parameters can be better defined such as to avoid unnecessary steps of exploration or exploitation. Discrete response surfaces are prepared with the simultaneous variation of 2 of the 4 geometrical parameters, as listed on Table 1; the tested points are equally spaced. The production of those surfaces shown in Figure 5 is of relatively low time cost, but this kind of analysis is only reasonable for domains with low number of dimensions. The surfaces are not used for the production of interpolation functions of any kind.

For the evaluated set of geometrical parameters, only one minimum and one maximum are noticed in the tested domain (resembling the surfaces presented by [5] in an aerodynamic optimization). It is assumed that a similar behavior is present when all the variables are analyzed simultaneously, with zero to a few local minima. The *gbest* topology

Table 1: Discrete response surfaces parameters.

#	1	2	3
L/d	1.00	[0.25; 1.75]	[0.25; 1.75]
k	0.50	[0.00; 1.00]	0.30
j_F	(0.00; 1.00)	$\sqrt{2}-1$	$\sqrt{2}-1$
j_B	(0.00; 1.00)	$\sqrt{2}-1$	[0.00; 1.00]
points	15×15	16×11	16×11

suits these type of function and the influence of the settings in the final result is small. Empirical tests are thus performed for known functions with those characteristics, allowing to find settings adapted to the present context. This study is performed with those functions because of the cheap evaluation and by the fact that once the value and the position of the minimum are previously defined, the performance of the optimizer is evaluated based on the expected final result and the rate of success of the optimization can be measured.

2.4.3. Performance study

From the observed discrete response surfaces, the Michalewicz test function [32] at low dimension is used as test case for the selection of the optimizer parameters. An unimodal version is also proposed, in 2 and 3 dimensions. Both functions are presented on Table 2. Stepness factor m is set to 10 for the original function so that the tests also contemplate very localized minima. The factor m equals 1 for the modified version.

Performance maps are produced with multiple values of the cognitive and the social factors: 19 values of c_1 and c_2 (total of 361 combinations) in (0.0; 2.5); and the inertia factor is maintained, $c_w = 0.6$.

Since the chosen optimization is an stochastic technique, a total of $N = 10{,}000$ optimization runs are performed for each pair of values within the set of parameters and the statistics of the obtained distributions are used to represent the influence of the factors. For those analyses, a number of 25 (2D) or 27 (3D) particles are used and their initial positioning is a Cartesian mesh of equally spaced elements points (5×5 or $3 \times 3 \times 3$). As the function optima are known, the optimizations are stopped when the absolute difference of it with the global best is smaller than 0.001. The maximum number of iterations is fixed at $T_{max} = 200$. If the final best is not within the range of precision, the run is considered a failure. As the number of total iterations is restrictive, a high rate of failure may not be solely caused by a bad choice of parameters. However, for the intended use of the optimization in this article, the selected maximum value is already beyond the desirable number of iterations, in a sense that, a successful but long run is unfeasible.

The results are presented on Figure 7 with the average number of function evaluations in the optimization for the total number of runs, and the failure rate (number of runs that did not found the global best divided by N) for every tested pair of parameters. In all 3 configurations, the cognitive factor (c_1) has low impact in the performance, what is probably due to the topology (every particle has the access to the best result of the complete swarm). A good trade off of function evaluations and small failure rate shall be obtained on the center of the map (about 1200 evaluations for Michalewicz in 2D, 250 for modified Michalewicz in 2D and 450 for modified Michalewicz in 3D). Based on those results, the parameters for the optimization are chosen as $c_w = 0.6$ and $c_1 = c_2 = 1.2$, values within the stability regions proposed in [33] and [31] and fairly consistent even for harder problems than those we are dealing with (such as Michalewicz).

Considering the results for the modified Michalewicz in 3D, the configuration that most resembles the expected objective functions (single minimum, more than 2 dimensions), the number of iterations for achieving the optimum with the selected factors is about 20 (the average number of functions evaluations divided by the number of particles).

Similar technique is applied for the study of the number of agents to be selected. For a number of particles from 1 to 40, placed on the search space using a Latin Hypercube Sampling (LHS), the same 10,000 runs are evaluated. The obtained evaluations of mean number of function evaluations, normalized number of iterations (mean number of iterations necessary to convergence divided by the max number of iterations) and rate of success (number of runs that converged divided by the total number of runs) are presented on Figure 8.

It is noted that, for a good success rate at a tenable number of iterations (less than 30, $T/T_{max} = 0.15$), at least 30 particles must be used. For the modified Michalewicz, after 20 particles, the increase in the number of particles does not affect the success rate. According to those result, the following optimizations are performed with 36 particles.

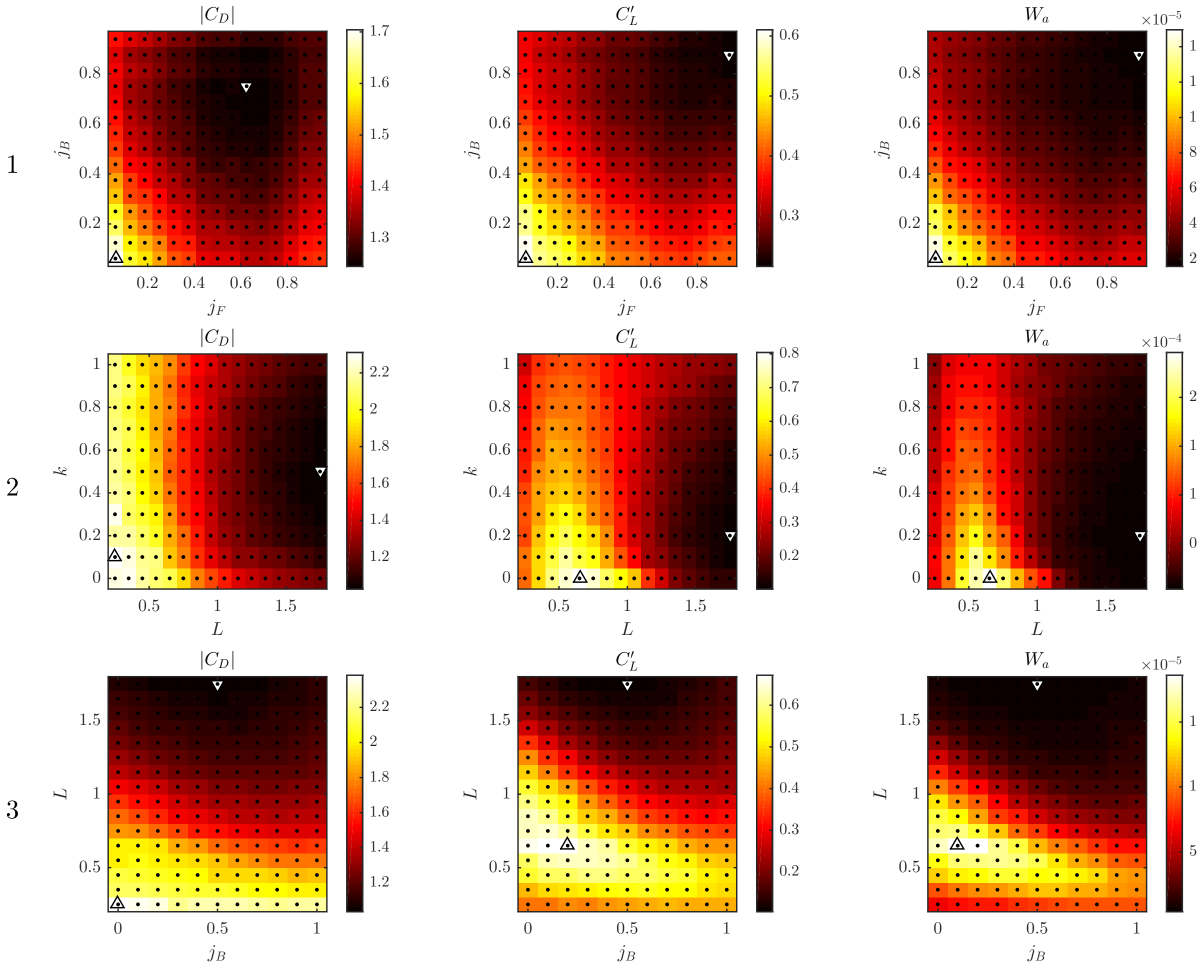

Figure 5: Discrete response surfaces for $|C_D|$ (left), C'_L (center) and W_a (right) for the 3 pairs of variables - for every case, the remaining geometrical parameters are fixed. The dots represent the coordinates of the calculated points; the up-pointing triangle is placed at the maximum level and the down-pointing triangle at the minimum.

3. Results

The optimization procedure presented in the previous section is now applied to the unsteady flows over obstacles.

Several optimizations are performed for 3D design space (j_F, j_B and k). The aspect ratio is either fixed or constrained to obtain a selected cross section surface or perimeter. The 2 later properties are calculated via the discrete sum of surface and length elements of each Bezier arc (2000 per arc). As both quantities are monotonic laws of L, bisection method is applied for each particle in order to obtain the AR that corresponds to the desired surface or contour.

Optimizations were performed in 4D, using AR as a parameter. However, the influence of the length of the obstacle surpasses the remaining geometrical parameters in such a way that all the optimizations are rapidly reduced to 3D, so these runs are not presented here. The swarm converged to the maximum L when minimum drag or acoustic power were aimed.

The search space boundaries are the parameters limits issued from the definition of the geometry, what traduces to the design space $[0;1]^3$. The starting points of the particles are the nodes of an equally distributed rectangular grid of the design space ($4 \times 3 \times 3$ nodes).

Although several other cases were evaluated, only the results for minimum mean drag and acoustic power are presented in details for conciseness. Other results are evoked in the following sections

Table 2: Test functions.

Function	Equation	Search space	Global minimum
Michalewicz $(m = 10)$	$\sum_{i=0}^{D} sin(x_i)sin(\frac{ix_i^2}{\pi})^{2m}$	$[0;\pi]^2$	-1.8013 at $[2.20319; 1.57049]$
mod. Michalewicz $(m = 1)$	$\sum_{i=0}^{D} sin(x_i)sin(\frac{x_i^2}{\pi})^{2m}$	$[0;\pi]^2$	-1.6819 at $[2.07169]^2$
mod. Michalewicz $(m = 1)$	$\sum_{i=0}^{D} sin(x_i)sin(\frac{x_i^2}{\pi})^{2m}$	$[0;\pi]^3$	-2.5228 at $[2.07169]^3$

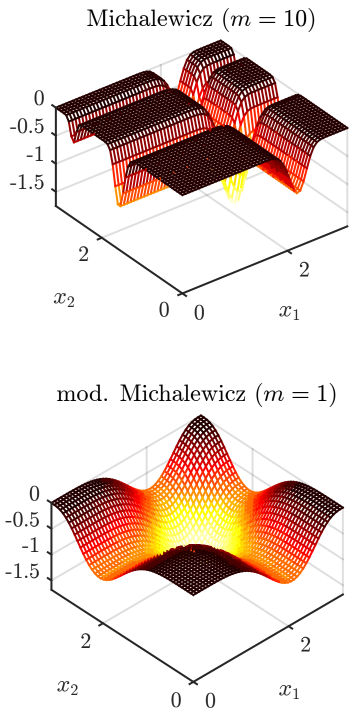

Figure 6: Test functions in 2D. For better visualization, the colormap is inversed from the rest of the images on this document

Table 3: List of performed optimizations.

AR	min C_D	min W_a
1.5	# 1	# 4
AR for $S = \pi/4\ d^2$	# 2	# 5
AR for $C = \pi d$	# 3	# 6

serving as a quantitative reference for the detailed cases. The conditions and objectives of those optimizations are summarized on Table 3. The length of $L = 1.5d$ is chosen to avoid the possible peaks of lift fluctuation at reduced aspect ratio, as the one reported by Inasawa et al. [25] for a rectangular section. When the length is not fixed, only the shapes that present either the surface or the perimeter of the circular section are considered.

The convergence of the swarm is illustrated by Figure 9. For all runs, the final best is found before 25 iterations. As it can be seen on the evolution of the mean velocity (mean of the velocity norm of all the members of the swarm in an specific iteration), the convergence is fast but there was not enough time for the swarm to arrive, in average, to the geometrical resolution of the calculation (limited to a variation of 0.001 of any parameter) based on the CFD mesh refinement. However, the small variation of the best result infers that further analysis would not give relevant improvements in the results. The total reduction of the cost function from the initial evaluations is lower than 10%, specially for the mean drag (optimizations 1 to 3), what may be explained by the use of a relatively large number of particles for such reduced number of dimensions, condition that results in a significant knowledge of the design space even at the initial iterations. Running the optimization procedure with a smaller number of particles (12) revealed lower computational time but the solution was depreciated (slightly higher W_a). That latter feature may be also linked to the topology with full communication between particles.

Despite the small gain for the selected objective functions, the advantages of performing the optimization also reside in the achieved precision. The parameters that result in the final best are signif-

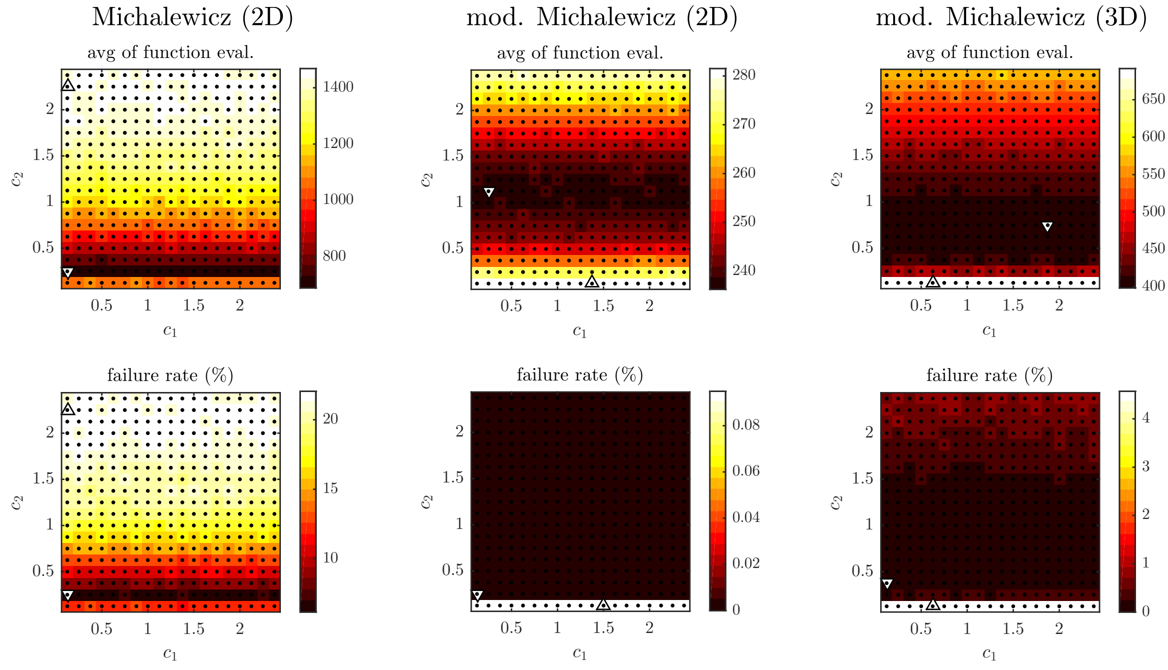

Figure 7: Average number of function evaluations (top) and the failure rate (down). The up-pointing triangle is placed at the maximum level and the down-pointing triangle at the minimum.

icantly different from the ones of the initial best (smaller response obtained at the starting positions), as presented by the euclidean distance of those points listed in Table 4, recalling that the maximum possible distance is of $\sqrt{3}$. The number of evaluations of the objective function to achieve a similar precision without the use of optimization would be of 1000^3.

Table 4: Comparison of initial and final best results.

#	$\frac{\text{initial best}}{\text{final best}}$	distance
1	-1%	0.136
2	-6%	0.424
3	-2%	0.174
4	-7%	0.186
5	-2%	0.473
6	-8%	0.070

The geometrical and aeroacoustic results are discussed in the next sections. Simulations of ellipses at similar lengths are also performed and serve as reference for the optimal results. The obtained optimal shapes and the associated flows are illustrated on Figures 10 and 11, respectively.

3.1. Minimum drag

The corresponding geometrical and aeroacoustic properties of the shapes minimizing drag are presented on Table 5. At fixed length, there is a small reduction of the mean drag when compared to the elliptical section of same length (1.3%). There are reductions of 5.9% at equal surface and 0.9% at same total contour when compared to the circular cross section.

At fixed length, the geometry can be interpreted as an inflated circle. Since the perimeter is a very restrictive constraint at fixed d, the obtained result at fixed C is not so different from the circle itself, what can be also noted on the slight variation of the quantities. Even so, the optimization routine was able to successfully find a geometry with smaller drag.

For fixed cross-surface, the smallest drag is obtained with a drop shaped geometry. This result can be justified by two phenomenons: as presented in other studies, the increase of the length is accompanied by a severe reduction of drag [25] in this regime, what can only be achieved at constrained S with sharp edges (j_F or j_B close to 0); also, there is a smaller influence of the pressure at the downstream part of the geometry (depression zone after

Table 5: Geometrical and aeroacoustical quantities for minimum mean drag shapes and elliptical cylinders.

	min C_D fixed AR	min C_D fixed S	min C_D fixed C	ellipse ($AR = 1.0$)	ellipse ($AR = 1.5$)
j_F	0.561	0.388	0.386	0.414	0.414
j_B	0.475	0.000	0.359	0.414	0.414
k	0.519	0.277	0.526	0.500	0.500
L/d	1.500	1.363	1.024	1.000	1.500
$\lvert C_D \rvert$	1.072	1.229	1.296	1.307	1.086
C'_L	0.143	0.327	0.333	0.338	0.166
$C'_D \times 10^1$	0.025	0.037	0.156	0.157	0.031
S_t	0.182	0.164	0.191	0.190	0.183
$W_a \times 10^5$	0.725	3.434	4.180	4.275	0.986

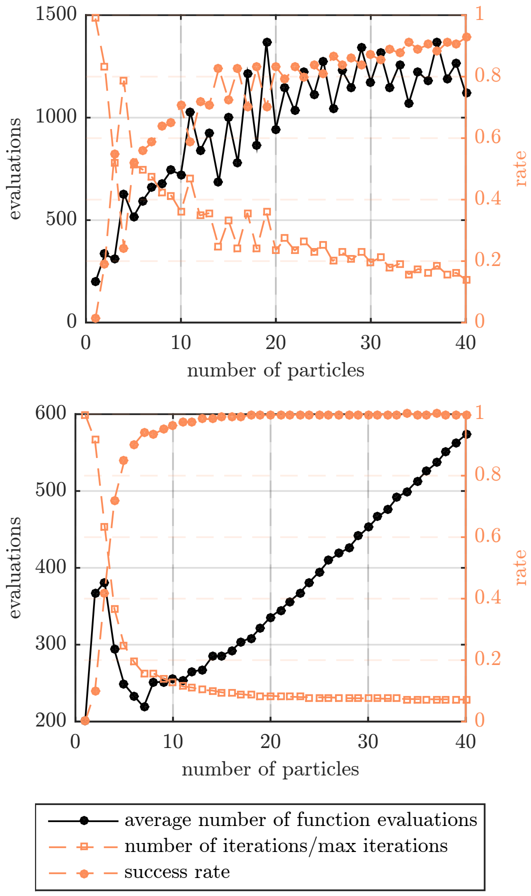

Figure 8: Influence of the number of particles for Michalewicz in 2D (right) and modified Michalewicz in 3D (left).

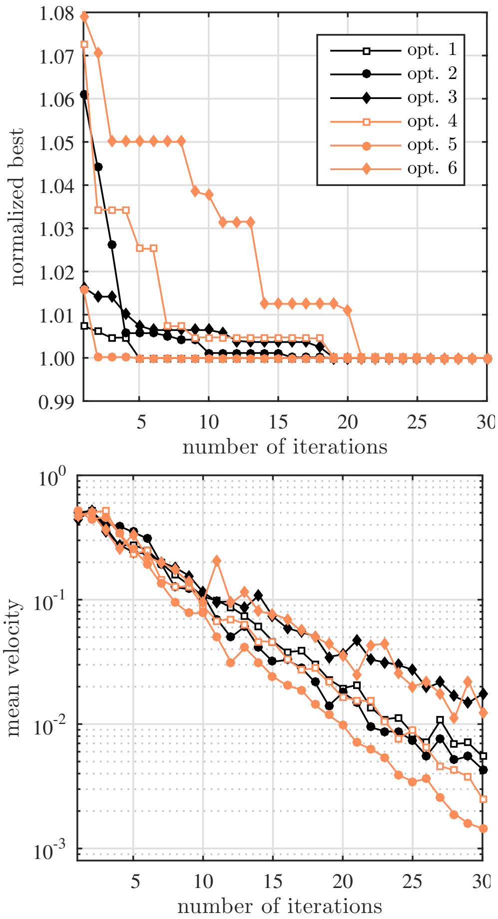

Figure 9: Convergence history: evolution of the normalized best (current best result divided by the final best) on the left and evolution of the mean velocity of the swarm (average of the velocity norm of all particles) on the right.

$x = kL$) due to the increased boundary angle, such as in the streamlined bodies, even if the flow sepa-

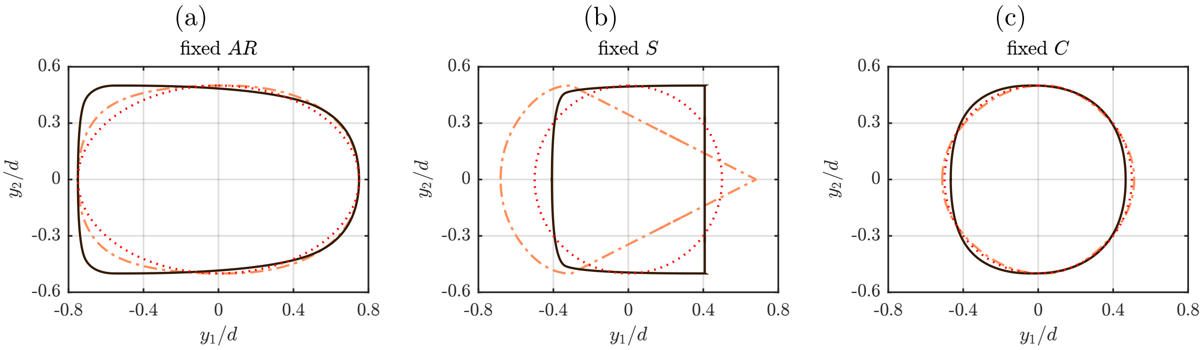

Figure 10: Comparison of optimal shapes for minimum drag (dash-dotted lines) and minimum acoustic power (full lines) at fixed aspect ratio (a), fixed surface (b) and fixed contour (c). Dotted lines are representations of ellipses of AR = 1.5 (a) and AR = 1.0 (b and c).

ration is still present. In this manner, it's possible that concave surfaces, that are by definition of the parametrization unreachable in our design space, would be able to further reduce the mean drag.

3.2. Minimum acoustic power

The corresponding geometrical and aeroacoustic properties of the shapes minimizing the acoustical emission are presented on Table 6. At $AR = 1.5$, the optimized section induces half the acoustic power of an ellipse of same length, that means -3.0 dB. Performance of the best shapes at fixed surface and contour are of -1.2 and -0.6 dB using the circular section as reference. At the 3 cases, there is an increase in the mean drag with respect to the ellipse, what emphasis the separation of the two phenomenons. A similar dispute between acoustic and drag minimization was also noted by Beigmoradi et al. [7].

For all of the geometries minimizing W_a, there is an increase in the bluffness of the bodies, that is increase of j_B, followed by a slight modification in the topology of the wake. The vortex formation is pushed in the downstream direction when compared to the flow in the presence of ellipses of similar aspect ratio (see Figure 11).

Optimizations procedures searching the minimum lift fluctuation (C'_L) resulted in very similar geometries. One conclusion is, as expected, that the lift fluctuations are the major component of the acoustic emission at this regime, once it is at least one order higher than the drag contribution and the one that is most crucially influenced by the shape, notably when compared to the Strouhal.

It's important to note that the chosen reference for all comparisons (the elliptical section), is already fairly optimal if compared to the other possible geometries that reside within the proposed design space and constraints (such as lozenges and triangles). Even so, there are reasonable gains, specially in terms of W_a. In that manner of emphasizing the potential of such routines, optimizations are performed for maximizing C_D and W_a, using the inverse of the correspondent quantity as cost function. The ratios between the associated extrema are presented at Table 7. The maximum W_a is a backward facing triangle ($k = 0$, $j_B = 0$), independently of the constraint. Simultaneously, cross comparison is performed with the presented values concerning minimum drag and minimum acoustic power.

When geometries that minimize different quantities are confronted, their variance response to the shape is once again highlighted. At fixed aspect ratio, for instance, the section that minimizes the drag produces 1.7 dB more noise than the min W_a. For the opposite situation, ratio between the drag of the shape with min W_a and the minimum drag, 3% difference in noted. Considering that the human perception can differentiate noise only after 1 dB of difference, one may imply that for the test case configuration, the mean drag optimization may be also sufficient for the acoustic point of view. However, the restrictiveness of the performed study in terms of shape (constrained length L and fixed height d) and flow regime confines this conclusion.

The ratios between maximum and minimum behaviors show that even respecting a set of strict continuity and geometrical constraints, the selected geometry can produce up to 8 dB more noise than a

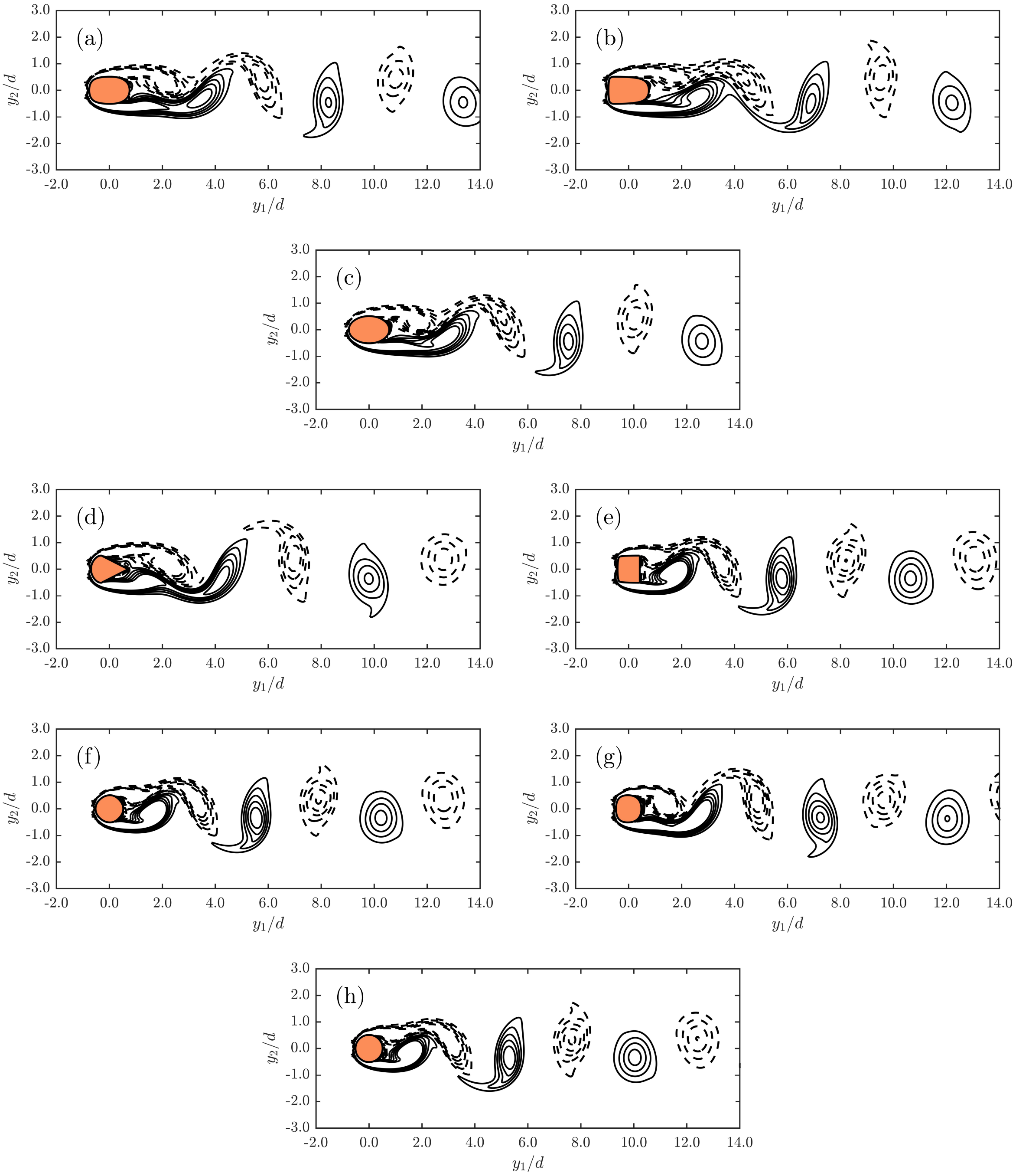

Figure 11: Snapshots of instantaneous vorticity for optimized and canonical geometries: optimized geometry for minimum C_D (a) and minimum W_a (b) at fixed length $L/d = 1.5$; optimized geometry for minimum C_D (d) and minimum W_a (e) at fixed cross section area $S = \pi/4\ d^2$; optimized geometry for minimum C_D (f) and minimum W_a (g) at fixed contour $C = \pi d$; and ellipses of $AR = 1.5$ (c) and $AR = 1.0$ (h). The contour intervals are $0.4\ U_\infty/d$ and dashed lines represent negative values.

Table 6: Geometrical and aeroacoustical quantities for minimum acoustic power shapes and elliptical cylinders.

	min W_a fixed AR	min W_a fixed S	min W_a fixed C	ellipse ($AR = 1.0$)	ellipse ($AR = 1.5$)
j_F	0.656	0.833	0.520	0.414	0.414
j_B	0.603	0.329	0.483	0.414	0.414
k	0.136	1.000	0.465	0.500	0.500
L/d	1.500	0.815	0.933	1.000	1.500
$\|C_D\|$	1.107	1.377	1.311	1.307	1.086
C'_L	0.120	0.296	0.316	0.338	0.166
$C'_D \times 10^1$	0.017	0.224	0.154	0.157	0.031
S_t	0.174	0.185	0.188	0.190	0.183
$W_a \times 10^5$	0.492	3.209	3.699	4.275	0.986

Table 7: Comparison of minimum and maximum results of optimized geometries

constraint	$\frac{C_D(\min W_a)}{\min C_D} - 1$	$\frac{W_a(\min C_D)}{\min W_a}$	$\frac{\max C_D}{\min C_D} - 1$	$\frac{\max W_a}{\min W_a}$
fixed AR	3%	1.7 dB	51%	16.5 dB
fixed S	12%	0.3 dB	32%	7.9 dB
fixed C	1%	0.5 dB	40%	9.3 dB

optimized version. Since the weight of each aspect is a function of the final application, the importance of this comparison resides in exemplifying the risk of not considering the acoustic aspects on product design.

4. Concluding remarks

Optimization techniques are largely used in engineering problems, what also globes aerodynamics. Although the numerous applications, the use is mainly associated with both strong flow hypothesis and surrogate models. On this work, an optimization framework based on parallel evaluations of the direct solution of Navier-Stokes equations and a single equation acoustic estimation based on Curle's analogy was reported. Simultaneously, results concerning the most common objective in the aerodynamic aspect, the mean drag, are confronted with the shapes obtained when the minimum aeroacoustic emission is searched.

The use of an stochastic optimization technique (PSO) is normally associated with an elevated number of function evaluations. As noted from the characteristics of the current response surface in contrast with the typical problems associated with the use of a meta-heuristic optimization routine, the conclusion is that they must not be ignored even without the use of surrogate models. The use of a preliminary study of the optimizer settings and an optimized mesh allowed the use of such kind of methodology and to profit from its robustness. The flexibility and simplicity of the chosen parametrization, that resulted in a smooth low-dimension design space, were important factors for the representativeness and the success of the performed optimizations. Moreover, the possibility to use a single mesh due to the application of an IBM technique must be highlighted.

A maximum decrease of 6% of the mean drag relatively to a similar elliptical section was achieved. Also, obtained results presented a reduction up to 3 dB when compared to ellipses of same length, behavior originated mainly from the reduction of lift fluctuations. Less noisy geometries are of increased bluffness and, as its portrayed in previous publications, the aspect ratio surpassed all other geometrical parameters in terms of regulating the acoustic emission. Additionally, it must be emphasized that for all the tested constraints, the shape that has minimum drag is different from the one that produces less noise. Thus, care must be taken in order to keep the W_a reduced.

A large variation of the acoustic quantity is noted when both extrema (max and min) are compared. This behavior represents simultaneously the potential of the shape optimization in terms of acoustic emission, even at a such specific conditions, and the risk of ignoring the aeroacoustic behavior in engineering design.

5. Acknowledgements

Computations have been performed on the supercomputer facilities of the Mésocentre de Calcul de Poitou Charentes.

References

[1] D. E. Goldberg, Genetic Algorithms in Search, Optimization and Machine Learning, 1st Edition, Addison-Wesley Longman Publishing Co., Inc., Boston, MA, USA, 1989.

[2] R. Storn, K. Price, Differential evolution – a simple and efficient heuristic for global optimization over continuous spaces, Journal of Global Optimization 11 (4) (1997) 341–359. `doi:10.1023/A:1008202821328`.
URL `http://dx.doi.org/10.1023/A:1008202821328`

[3] M. Dorigo, V. Maniezzo, A. Colorni, Ant system: Optimization by a colony of cooperating agents, Trans. Sys. Man Cyber. Part B 26 (1) (1996) 29–41. `doi:10.1109/3477.484436`.
URL `http://dx.doi.org/10.1109/3477.484436`

[4] J. Kennedy, R. Eberhart, Particle swarm optimization, in: Neural Networks, 1995. Proceedings., IEEE International Conference on, Vol. 4, 1995, pp. 1942–1948 vol.4. `doi:10.1109/ICNN.1995.488968`.

[5] S. Krajnovic, Shape optimization of high-speed trains for improved aerodynamic performance, in: Proceedings of the Institution of Mechanical Engineers, Part F: Journal of Rail and Rapid Transit, 2009, pp. 439–452.

[6] C. Praveen, R. Duvigneau, Low cost pso using metamodels and inexact pre-evaluation: Application to aerodynamic shape design, Computer Methods in Applied Mechanics and Engineering 198 (9) (2009) 1087 – 1096. `doi:https://doi.org/10.1016/j.cma.2008.11.019`.
URL `http://www.sciencedirect.com/science/article/pii/S0045782508004155`

[7] S. Beigmoradi, H. Hajabdollahi, A. Ramezani, Multi-objective aero acoustic optimization of rear end in a simplified car model by using hybrid robust parameter design, artificial neural networks and genetic algorithm methods, Computers & Fluids 90 (Supplement C) (2014) 123 – 132. `doi:https://doi.org/10.1016/j.compfluid.2013.11.026`.
URL `http://www.sciencedirect.com/science/article/pii/S0045793013004659`

[8] S. B. Yao, D. L. Guo, Z. X. Sun, D. W. Chen, G. W. Yang, Parametric design and optimization of high speed train nose, Optimization and Engineering 17 (3) (2016) 605–630. `doi:10.1007/s11081-015-9298-6`.
URL `http://dx.doi.org/10.1007/s11081-015-9298-6`

[9] C. H. K. Williamson, Vortex dynamics in the cylinder wake, Annual Review of Fluid Mechanics 28 (1) (1996) 477–539. `arXiv:https://doi.org/10.1146/annurev.fl.28.010196.002401`, `doi:10.1146/annurev.fl.28.010196.002401`.
URL `https://doi.org/10.1146/annurev.fl.28.010196.002401`

[10] A. Roshko, Perspectives on bluff body aerodynamics, Journal of Wind Engineering and Industrial Aerodynamics 49 (1) (1993) 79 – 100. `doi:https://doi.org/10.1016/0167-6105(93)90007-B`.
URL `http://www.sciencedirect.com/science/article/pii/016761059390007B`

[11] W. F. King, E. Pfizenmaier, An experimental study of sound generated by flows around cylinders of different cross-section, Journal of Sound and Vibration 328 (3) (2009) 318–337.
URL `http://www.sciencedirect.com/science/article/pii/S0022460X09006221`

[12] S. R. L. Samion, M. S. M. Ali, A. Abu, C. J. Doolan, R. Z.-Y. Porteous, Aerodynamic sound from a square cylinder with a downstream wedge, Aerospace Science and Technology 53 (Supplement C) (2016) 85 – 94. `doi:https://doi.org/10.1016/j.ast.2016.03.007`.
URL `http://www.sciencedirect.com/science/article/pii/S1270963816301006`

[13] S. Becker, C. Hahn, M. Kaltenbacher, R. Lerch, Flow-induced sound of wall-mounted cylinders with different geometries, AIAA Journal 46 (9) (2008) 2265–2281. `doi:10.2514/1.34865`.
URL `https://doi.org/10.2514/1.34865`

[14] D. Goldstein, R. Handler, L. Sirovich, Modeling a no-slip flow boundary with an external force field, Journal of Computational Physics 105 (2) (1993) 354 – 366. `doi:http://dx.doi.org/10.1006/jcph.1993.1081`.
URL `http://www.sciencedirect.com/science/article/pii/S0021999183710818`

[15] C. S. Peskin, The immersed boundary method, Acta Numerica 11 (2002) 479–517. `doi:10.1017/S0962492902000077`.

[16] F. Margnat, V. Morinière, Y. Gervais, Noise radiated by flow impingement on a flat plate using DNS with a virtual boundary method, International Journal of Aeroacoustics 4(1+2) (2005) 117–134.

[17] C. Degand, C. Farhat, A three-dimensional torsional spring analogy method for unstructured dynamic meshes, Computers & Structures 80 (3–4) (2002) 305 – 316. `doi:http://dx.doi.org/10.1016/S0045-7949(02)00002-0`.
URL `http://www.sciencedirect.com/science/article/pii/S0045794902000020`

[18] A. de Boer, M. van der Schoot, H. Bijl, Mesh deformation based on radial basis function interpolation, Computers & Structures 85 (11–14) (2007) 784 – 795, fourth {MIT} Conference on Computational Fluid and Solid Mechanics. `doi:http://dx.doi.org/10.1016/j.compstruc.2007.01.013`.
URL `http://www.sciencedirect.com/science/article/pii/S0045794907000223`

[19] N. Curle, The influence of solid boundaries upon aerodynamic sound, Proceedings of the Royal Society of London A: Mathematical, Physical and Engineering Sciences 231 (1187) (1955) 505–514. `arXiv:http://rspa.royalsocietypublishing.org/content/231/1187/505.full.pdf`, `doi:10.1098/rspa.1955.0191`.

URL http://rspa.royalsocietypublishing.org/content/231/1187/505

[20] M. J. Lighthill, On sound generated aerodynamically i. general theory, Proceedings of the Royal Society of London A: Mathematical, Physical and Engineering Sciences 211 (1107) (1952) 564–587. arXiv:http://rspa.royalsocietypublishing.org/content/211/1107/564.full.pdf, doi:10.1098/rspa.1952.0060. URL http://rspa.royalsocietypublishing.org/content/211/1107/564

[21] F. Margnat, Hybrid prediction of the aerodynamic noise radiated by a rectangular cylinder at incidence, Computers & Fluids 109 (2015) 13 – 26. doi:http://dx.doi.org/10.1016/j.compfluid.2014.12.006. URL http://www.sciencedirect.com/science/article/pii/S0045793014004691

[22] S. Laizet, E. Lamballais, High-order compact schemes for incompressible flows: A simple and efficient method with quasi-spectral accuracy, J. Comput. Phys. 228 (16) (2009) 5989–6015. doi:10.1016/j.jcp.2009.05.010. URL http://dx.doi.org/10.1016/j.jcp.2009.05.010

[23] F. Margnat, V. Morinière, Behaviour of an immersed boundary method in unsteady flows over sharp-edged bodies, Computers & Fluids 38 (6) (2009) 1065 – 1079. doi:https://doi.org/10.1016/j.compfluid.2008.09.013. URL http://www.sciencedirect.com/science/article/pii/S0045793008002326

[24] O. Inoue, N. Hatakeyama, Sound generation by a two-dimensional circular cylinder in a uniform flow, Journal of Fluid Mechanics 471 (2002) 285–314. doi:10.1017/S0022112002002124.

[25] A. Inasawa, M. Asai, T. Nakano, Sound generation in the flow behind a rectangular cylinder of various aspect ratios at low mach numbers, Computers & Fluids 82 (Supplement C) (2013) 148 – 157. doi:https://doi.org/10.1016/j.compfluid.2013.05.006. URL http://www.sciencedirect.com/science/article/pii/S0045793013001928

[26] Y. Shi, R. Eberhart, A modified particle swarm optimizer, in: Evolutionary Computation Proceedings, 1998. IEEE World Congress on Computational Intelligence., The 1998 IEEE International Conference on, IEEE, 1998, pp. 69–73.

[27] R. Poli, J. Kennedy, T. Blackwell, Particle swarm optimization, Swarm Intelligence 1 (1) (2007) 33–57. doi:10.1007/s11721-007-0002-0. URL http://dx.doi.org/10.1007/s11721-007-0002-0

[28] L. Dalcín, R. Paz, M. Storti, J. D'Elía, Mpi for python: Performance improvements and mpi-2 extensions, Journal of Parallel and Distributed Computing 68 (5) (2008) 655 – 662. doi:https://doi.org/10.1016/j.jpdc.2007.09.005. URL http://www.sciencedirect.com/science/article/pii/S0743731507001712

[29] M. Clerc, Particle Swarm Optimization, ISTE, 2006.

[30] M. R. Bonyadi, Z. Michalewicz, Particle swarm optimization for single objective continuous space problems: A review, Evolutionary Computation 25 (1) (2017) 1–54, pMID: 26953883. arXiv:https://doi.org/10.1162/EVCO_r_00180, doi:10.1162/EVCO_r_00180. URL https://doi.org/10.1162/EVCO_r_00180

[31] Q. Liu, Order-2 stability analysis of particle swarm optimization, Evolutionary computation 23 (2) (2015) 187–216.

[32] X.-S. Yang, Engineering Optimization: An Introduction with Metaheuristic Applications, John Wiley & Sons, 2010, Ch. Test problems in optimization.

[33] I. C. Trelea, The particle swarm optimization algorithm: convergence analysis and parameter selection, Information Processing Letters 85 (6) (2003) 317 – 325. doi:https://doi.org/10.1016/S0020-0190(02)00447-7. URL http://www.sciencedirect.com/science/article/pii/S0020019002004477

[34] E. J. Avital, N. D. Sandham, K. H. Luo, Stretched cartesian grids for solution of the incompressible navier–stokes equations, International Journal for Numerical Methods in Fluids 33 (6) (2000) 897–918. doi:10.1002/1097-0363(20000730)33:6<897::AID-FLD37>3.0.CO;2-4. URL http://dx.doi.org/10.1002/1097-0363(20000730)33:6<897::AID-FLD37>3.0.CO;2-4

[35] A. Sohankar, C. Norberg, L. Davidson, Low-reynolds-number flow around a square cylinder at incidence: study of blockage, onset of vortex shedding and outlet boundary condition, International Journal for Numerical Methods in Fluids 26 (1) (1998) 39–56. doi:10.1002/(SICI)1097-0363(19980115)26:1<39::AID-FLD623>3.0.CO;2-P. URL http://dx.doi.org/10.1002/(SICI)1097-0363(19980115)26:1<39::AID-FLD623>3.0.CO;2-P

[36] A. Roshko, On the Development of Turbulent Wakes from Vortex Streets, NACA technical report, National Advisory Committee for Aeronautics, 1953. URL https://books.google.fr/books?id=ZGBymQEACAAJ

[37] C. Norberg, Effects of reynolds number and a low-intensity freestream turbulence on the flow around a circular cylinder, Ph.D. thesis, Chalmers University of Technology (1987).

[38] M. Hammache, M. Gharib, An experimental study of the parallel and oblique vortex shedding from circular cylinders, Journal of Fluid Mechanics 232 (1991) 567–590. doi:10.1017/S0022112091003804.

[39] D. Barkley, R. D. Henderson, Three-dimensional floquet stability analysis of the wake of a circular cylinder, Journal of Fluid Mechanics 322 (1996) 215–241. doi:10.1017/S0022112096002777.

[40] B. Pier, On the frequency selection of finite-amplitude vortex shedding in the cylinder wake, Journal of Fluid Mechanics 458 (2002) 407–417. doi:10.1017/S0022112002008054.

[41] O. Posdziech, R. Grundmann, A systematic approach to the numerical calculation of fundamental quantities of the two-dimensional flow over a circular cylinder, Journal of Fluids and Structures 23 (3) (2007) 479 – 499. doi:https://doi.org/10.1016/j.jfluidstructs.2006.09.004. URL http://www.sciencedirect.com/science/article/pii/S0889974606001083

[42] L. Qu, C. Norberg, L. Davidson, S.-H. Peng, F. Wang, Quantitative numerical analysis of flow past a circular cylinder at reynolds number between 50 and 200, Journal of Fluids and Structures 39 (Supplement C) (2013) 347 – 370. doi:https://doi.org/10.1016/j.jfluidstructs.2013.02.007.

URL `http://www.sciencedirect.com/science/article/pii/S0889974613000388`

[43] R. Franke, W. Rodi, B. Schönung, Numerical calculation of laminar vortex-shedding flow past cylinders, Journal of Wind Engineering and Industrial Aerodynamics 35 (Supplement C) (1990) 237 – 257. `doi:https://doi.org/10.1016/0167-6105(90)90219-3`.
URL `http://www.sciencedirect.com/science/article/pii/0167610590902193`

[44] A. D. L. Sohankar, C. Norberg, Numerical simulation of unsteady flow around a square two dimensional cylinder, in: 12th Australasian Fluid Mechanics Conference, 1995, pp. 517–520.

[45] J. Robichaux, S. Balachandar, S. P. Vanka, Three-dimensional floquet instability of the wake of square cylinder, Physics of Fluids 11 (3) (1999) 560–578. `arXiv:https://doi.org/10.1063/1.869930`, `doi:10.1063/1.869930`.
URL `https://doi.org/10.1063/1.869930`

[46] A. Sharma, V. Eswaran, Heat and fluid flow across a square cylinder in the two-dimensional laminar flow regime, Numerical Heat Transfer, Part A: Applications 45 (3) (2004) 247–269. `arXiv:http://dx.doi.org/10.1080/10407780490278562`, `doi:10.1080/10407780490278562`.
URL `http://dx.doi.org/10.1080/10407780490278562`

[47] S. Sen, S. Mittal, G. Biswas, Flow past a square cylinder at low reynolds numbers, International Journal for Numerical Methods in Fluids 67 (9) (2011) 1160–1174. `doi:10.1002/fld.2416`.
URL `http://dx.doi.org/10.1002/fld.2416`

[48] N. M. P. T. Maekawa, Shape Interrogation for Computer Aided Design and Manufacturing, 1st Edition, Springer-Verlag Berlin Heidelberg, 2002. `doi:10.1007/978-3-642-04074-0`.

Appendix A. Simulation time reduction

In order to reduce the simulation time for the realization of the optimization routines, two convergence studies are performed for domain size and mesh refinement. For both studies, unless otherwise stated, 40,000 timesteps are considered with a timestep physical duration of $\Delta t = 0.0042 \times d/U_\infty$ and a Reynolds number of Re = 150. The domain is discretized by mesh elements of dimensions $\Delta y_1 = 1.953 \times 10^{-2}d$ in the flow direction and variable transverse size, with $\Delta y_2 = 1.125 \times 10^{-2}d$ at the center (mesh is stretched from the body center [34]).

The presented aerodynamic quantities are the statistics of the last simulated flow period, defined by subsequent peaks of the lift signal. Indicated domain dimensions are normalized by the obstacle's total height d. The geometry is a streamlined 2D body described by an ellipse until kL and a 2nd degree polynomial downstream both connected with same tangent, with $k = 0.4$ and $L = 2.0d$ (Figure A.12).

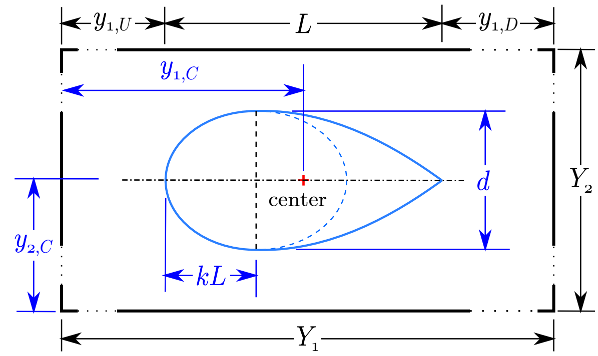

Figure A.12: Numerical domain and test geometry.

Appendix A.1. Domain convergence

Influence of upstream and downstream distance from domain limits are tested independently. As to maintain the size of the elements of the Cartesian mesh fixed, the number of elements is modified. For all configurations, the blockage ratio is fixed at 5% (reasonable blockage according to the results of Sohankar et al. [35]).

First test is performed for several upstream values while the downstream distance is fixed at $y_{1,D} = 27.00d$. The obtained mean drag, fluctuating lift and drag, and Strouhal number are presented in Table A.8 and Figure A.13. An horizontal, asymptotic behavior is noticed for each quantity, thus assessing convergence. An upstream distance of $11.00d$ (indicated with an arrow) is chosen as a good trade-off leading to a reduced calculation time; from the curves, the aerodynamic values to be obtained with this configuration are expected to be a overestimation.

Table A.8: Upstream convergence test

$y_{1,U}/d$	$\lvert C_D \rvert$	C'_L	C'_D	St
3.500	1.0954	0.1166	0.00070	0.189
6.313	1.0286	0.1160	0.00062	0.179
9.477	1.0074	0.1079	0.00059	0.176
11.000	1.0031	0.1088	0.00059	0.176
14.750	0.9982	0.1068	0.00058	0.175
21.000	0.9962	0.1067	0.00058	0.175

For the selected upstream distance of $11.00d$, five downstream distances are simulated (see Table A.9, Figure A.14). Based on the same criteria used for

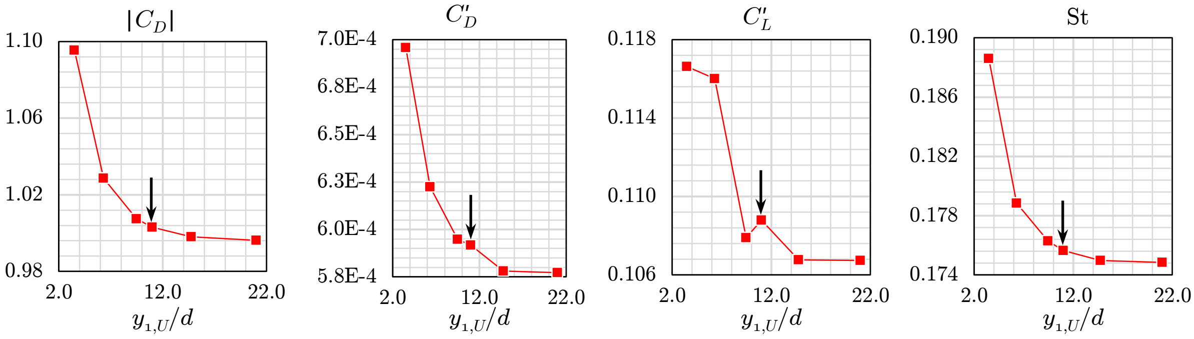

Figure A.13: Convergence of aerodynamic quantities as a function of the upstream distance. Arrows are placed at the selected value.

defining $y_{1,U}$, a downstream distance of $13d$ is selected for the final domain without major losses in the solution precision but reducing the number of calculation points.

Table A.9: Downstream convergence test.

$y_{1,D}/d$	$\lvert C_D\rvert$	C'_L	C'_D	St
7.000	1.0008	0.1135	0.00067	0.175
12.313	1.0033	0.1100	0.00058	0.176
17.000	1.0031	0.1088	0.00059	0.176
27.000	1.0032	0.1088	0.00059	0.176
32.000	1.0034	0.1089	0.00059	0.176

Based on this results, the final domain (used for all simulations presented in this article) has a total length of $Y_1 = 25.31d$ and the geometry center is at $y_{1,C} = 11.00d$ (that means $y_{1,U} = 10.50d$ and $y_{1,D} = 13.81d$ for a geometry of length $L = 1d$). Compared to the biggest domains that were tested, there is an average error of 0.8% for the mean drag, 2.2% for C'_L, 11.9% for C'_D and 0.6% for the Strouhal and a maximum local deviation of 2% for the mean velocity profiles.

Appendix A.2. Mesh convergence

A study of convergence in terms of mesh refinement is performed. The number of mesh points is modified by the same factor in both y_1 and y_2 directions, so the elements are simply scaled (note that mesh step changes affect the description of the geometry due to the use of the IBM).

For a better performance in the spectral solution of the Poisson equation, the number of points is chosen as a multiple of small prime factors + 1. For this study, the timestep physical duration of each simulation is modified to maintain numerical convergence. The results are presented at table A.11. Reference simulation (simulation 2 at table A.11) is the final configuration presented on previous section, within the following element size: $(\Delta y_1, \min\Delta y_2) = (0.002d, 0.001d)$.

From the performed tests, the factor 2 is considered reasonable (mesh 4). As demonstrated by the tests, the loss in geometrical precision is not followed by drastic modifications in the aerodynamic results. This behavior can be explained by the reduced Reynolds number used in this work. Final timestep duration is of $\Delta t = 0.0072 \times d/U_\infty$. When compared to the most refined solution, the associated errors are: 1.2% for the mean drag; 2.3% for C'_L; 8.5% for C'_D; 0.4% for the Strouhal number; 1% for the mean velocity profiles; and maximum local error of $8 \times 10^{-3} \times U_\infty$ for streamwise velocity RMS profiles.

The use of a not so refined numerical setup is a compromise for a reduced calculation time of the aerodynamic estimations without major losses in precision, so that the optimization is viable. The total CPU time equals 13% of the one obtained with the initial mesh for simulating an equal physical time.

Appendix A.3. Validation

Multiple flow configurations with the chosen domain and mesh properties are evaluated for canonical geometries.

Simulations are done for a range of Reynolds numbers considering geometries of $AR = 1.0$ (square and circular section) and for the evolution of the length of the rectangular section at fixed

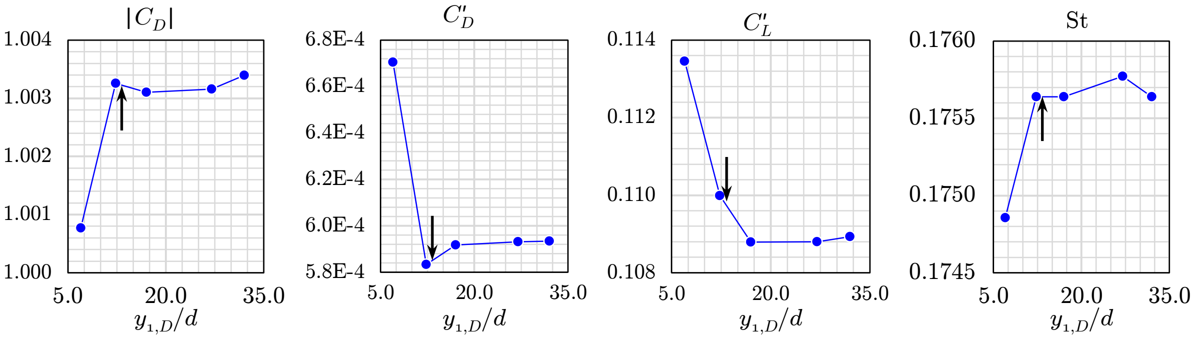

Figure A.14: Convergence of aerodynamic quantities as a function of the downstream distance. Arrows are placed at the length of the final mesh.

Table A.10: Final domain size.

case	$y_{1,U}/d$	$y_{1,D}/d$	$\|C_D\|$	C'_L	C'_D	St
$y_{1,U,max}$	21.0000	17.0000	0.9962	0.1067	0.00058	0.1749
$y_{1,D,max}$	11.0000	32.0000	1.0034	0.1089	0.00059	0.1756
final domain	10.0000	13.3125	1.0080	0.1101	0.00065	0.1763

Reynolds Re $=$ 150, so the capacity to compare geometries at fixed inlet conditions such as its performed on the optimization is proven. The results for 3 aerodynamic quantities are presented on Figure A.15 and compared to published values from references listed on Table A.12.

As expected from the performed convergence studies, the chosen configuration results in aerodynamic quantities larger than the values reported in the literature. As can be noted on the graph of the Strouhal number as a function of the Reynolds number for the square section (Figure A.15.b), the error decreases for a more refined grid (mesh 2). For rectangular sections of different lengths, Figure A.15.d, there is an offset of the estimated lift fluctuation for the shortest shapes (AR $<$ 0.5) for meshes 2 and 4 with respect to the literature data. Note that such short obstacles are not in the design space of any of the optimizations performed here.

This result assures the capacity of the chosen domain to represent the physics of the problem. Although the differences, the offset remains reasonable and, most importantly, the trends are kept for different configurations; that is, the same behavior of the reference values is maintained, what infers that comparing different shapes with this refinement is valid.

Appendix B. Geometry

Appendix B.1. The Bézier curve

A Bézier curve is a parametric curve based on the Bernstein polynomial that uses the position of control points:

$$\mathbf{r}(t) = \sum_{i=0}^{n} \mathbf{p}_i B_{i,b}(t), \qquad 0 \leqslant t \leqslant 1. \tag{B.1}$$

$$B_{i,n}(t) = \frac{n!}{i!(n-i)!}(1-t)^{n-i}t^i, \qquad i = 0, ..., n. \tag{B.2}$$

where $\mathbf{p}_i$ are the n control points (y_1, y_2) and $B_i, n(t)$ are the Bernstein polynomial. A big advantage of this kind of curve for the use in aerodynamic and aeroacoustics contexts is the possibility to obtain any desirable level of continuity by appropriate choice of the order. More details on properties of those curves are also available on [48].

Appendix B.2. Parametric obstacle

The obstacle is composed by a combination of 4 Bézier curves denoted as arcs $\widehat{A}$, $\widehat{B}$, $\widehat{C}$ and $\widehat{D}$ on Figure B.16, being $\widehat{A}$ and $\widehat{D}$ quadratic curves and

Table A.11: Mesh refinement.

#	n_1	n_2	factor	$\lvert C_D \rvert$	C'_L	C'_D	St
1	1945	769	0.667	1.0094	0.1101	0.00066	0.1764
2	1297	513	1.000	1.0080	0.1101	0.00065	0.1763
3	973	385	1.333	1.0031	0.1076	0.00065	0.1767
4	649	257	2.000	0.9970	0.1065	0.00060	0.1771
5	487	193	2.667	1.0093	0.1129	0.00070	0.1758

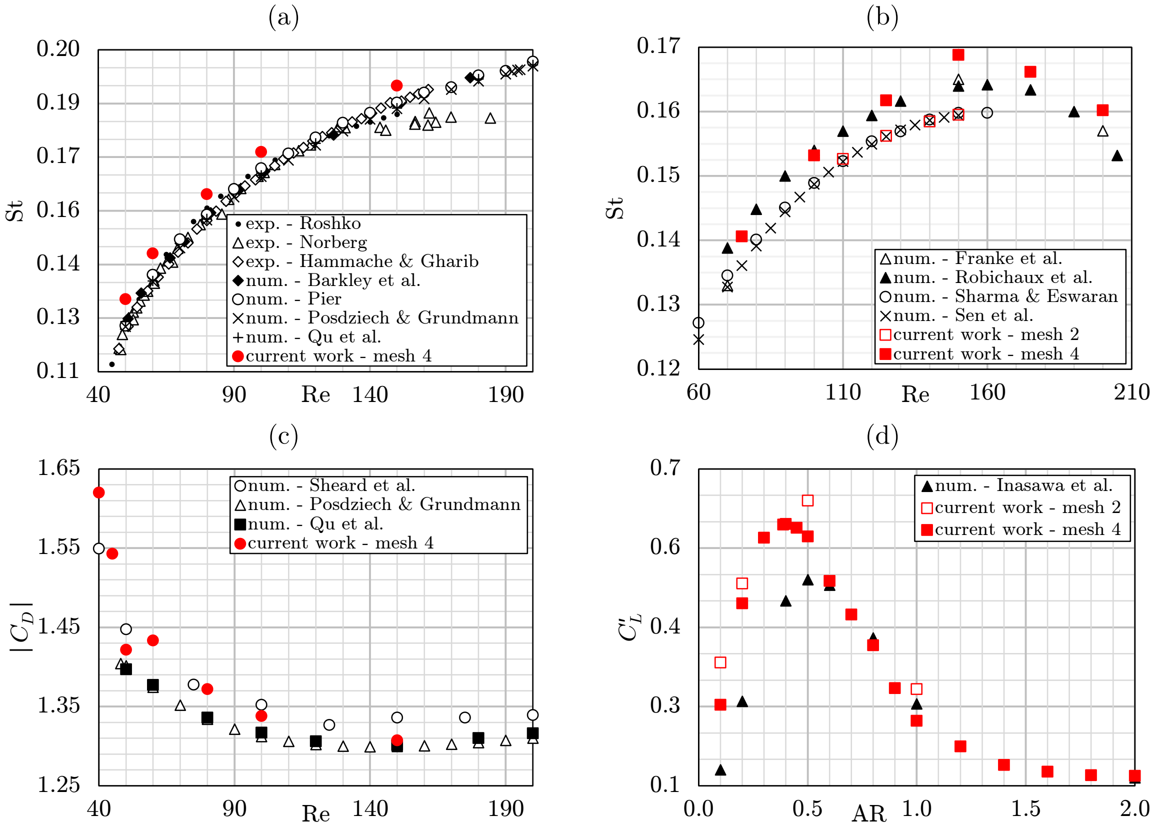

Figure A.15: Validation of the final mesh with canonical geometries: (a) Strouhal number versus Reynolds number for the circular section cylinder; (b) Strouhal number versus Reynolds number for the square section cylinder; (c) drag coefficient versus Reynolds number for the circular section cylinder; and (d) lift coefficient RMS level versus aspect ratio for the rectangular section cylinder.

$\widehat{B}$ and $\widehat{C}$ cubic curves, mirrored on the horizontal axis. It is circumscribed by a rectangle, represented by the points $M(0,0)$, $N(0,d/2)$, $O(kL,d/2)$, $P(L,d/2)$, $Q(L,0)$ and $R(kL,0)$.

The control points are placed so the final geometry shape respects the following geometrical constraints:

1. Length L and height $d/2$;
2. Symmetry in horizontal axis;
3. Tangency to the vertical axes at the beginning (M) and end (Q) of the obstacle
4. Position, tangency and curvature continuities (C^0, C^1 and C^2) at the connections of the 4 curves (for the exception when it's an edge - k, j_B and/or j_F are on their limits);
5. Tangency at the end of arc $\widehat{A}$/start of arc $\widehat{B}$ parallel to segment line $\overline{MO}$;
6. Tangency to the horizontal axis at the end of

Table A.12: List of sources for the final mesh and domain validation.

section	methodology & author
circular	exp. - Roshko (1954) [36]
	exp. - Norberg (1987) [37]
	exp. - Hammache & Gharib (1991) [38]
	2D num. - Barkley et al. (1996) [39]
	2D num. - Pier (2002) [40]
	2D num. - Posdziech & Grundmann (2007) [41]
	2D-3D num. - Qu et al. (2013) [42]
rectangular	2D num. - Franke et al. (1990) [43]
	2D num. - Sohankar et al. (1995) [44]
	2D num. - Robichaux et al. (1999) [45]
	2D num. - Sharma & Eswaran (2004) [46]
	2D num. - Sen et al. (2011) [47]
	2D num. - Inasawa et al. (2013) [25]

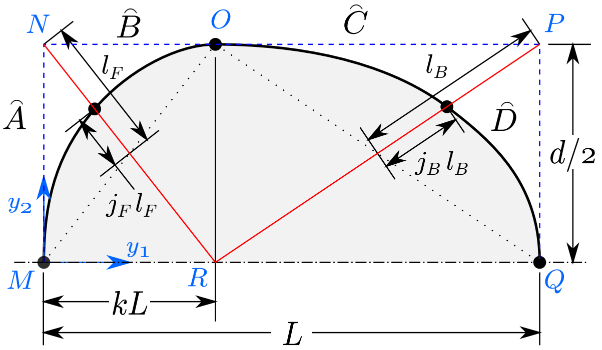

Figure B.16: Scheme of the parametrized geometry. The shape is convex and circumscribed by the rectangle MNPQ of length L and height $d/2$. The form is completely defined by 5 parameters: L, d, j_F, k and j_B. As d is fixed on this work, the aspect ratio L/d is the only parameter affecting the rectangle.

arc $\widehat{B}$/start of arc $\widehat{C}$ - at point O;

7. Infinity curvature radius at the end of arc $\widehat{B}$/start of arc $\widehat{C}$ - at point O;
8. Tangency at the end of arc $\widehat{C}$/start of arc $\widehat{D}$ parallel to segment line $\overline{OQ}$;
9. End of arc $\widehat{A}$ placed at the line segment $\overline{NR}$, at a normalized distance of $j_F \in [0, 1]$ from the intersection of $\overline{NR}$ with $\overline{MO}$;
10. End of arc $\widehat{C}$ placed at the line segment $\overline{PR}$, at a normalized distance of $j_B \in [0, 1]$ from the intersection of $\overline{PR}$ with $\overline{OQ}$;

Based on this constraints, geometry is completely defined by the 5 cited parameters. Parameters j_F and j_B allow the final result to be between a lozenge ($j_F = j_B = 0.0$) and a rectangle ($j_F = j_B = 1.0$) of dimensions L and d. The position of the control points are (where $y_{i,c,p}$ indicates the coordinate on direction i of the control-point number p of curve c):

Table B.13: Control points

curve	point	y_1	y_2
$\widehat{A}$	0	0	0
	1	0	$j_F d/2$
	2	$(1 - j_F)kL/2$	$(1 + j_F)d/4$
$\widehat{B}$	0	$y_{1,A,2}$	$y_{2,A,2}$
	1	$kL(1 - j_F)$	$d/2$
	2	$\begin{cases} 0 & \text{if } j_F = 1.0 \\ kL\{1 - j_F + & \text{otherwise} \\ \quad +[3j_F/(1 - j_F)^2] & \\ \qquad [1 - (1 + j_F)/2]^2\} & \end{cases}$	$d/2$
	3	kL	$d/2$
$\widehat{C}$	0	kL	$d/2$
	1	$\begin{cases} 0 & \text{if } j_B = 1.0 \\ L\{j_B + k(1 - j_B) + & \text{otherwise} \\ \quad -[3j_B(1 - k)/(1 - j_B)^2] & \\ \qquad [1 - (1 + j_B)/2]^2\} & \end{cases}$	$d/2$
	2	$L[k + (1 - k)j_B]$	$d/2$
	3	$L[k + (1 - k)(j_B + 1)/2]$	$(1 + j_B)d/4$
$\widehat{D}$	0	$y_{1,C,3}$	$y_{2,C,3}$
	1	L	$j_B d/2$
	2	L	0